

1  
2  
3 **Top of the Atmosphere Reflected Shortwave Radiative Fluxes from GOES-R**

4 Rachel T. Pinker<sup>1</sup>, Yingtao Ma<sup>1</sup>, Wen. Chen<sup>1</sup>, Istvan Laszlo<sup>2</sup>, Hongqing Liu<sup>3</sup>,  
5 Hye-Yun Kim<sup>3</sup> and Jamie Daniels<sup>2</sup>  
6

7 <sup>1</sup>Department of Atmospheric and Oceanic Science, University of Maryland, College Park, MD

8 <sup>2</sup>NOAA NESDIS Center for Satellite Applications and Research, College Park, MD

9 <sup>3</sup>I.M. Systems Group, Inc., Rockville, MD

10 Correspondence to: Rachel T. Pinker ([pinker@atmos.umd.edu](mailto:pinker@atmos.umd.edu))

11  
12 **Abstract.** Under the GOES-R activity, new algorithms are being developed at the National Oceanic and  
13 Atmospheric Administration (NOAA)/Center for Satellite Applications and Research (STAR) to derive  
14 surface and Top of the Atmosphere (TOA) shortwave (SW) radiative fluxes from the Advanced Baseline  
15 Imager (ABI), the primary instrument on GOES-R. This paper describes a support effort in the  
16 development and evaluation of the ABI instrument capabilities to derive such fluxes. Specifically, scene  
17 dependent narrow-to-broadband (NTB) transformations are developed to facilitate the use of observations  
18 from ABI at the TOA. Simulations of NTB transformations have been performed with MODTRAN4.3  
19 using an updated selection of atmospheric profiles and implemented with the final ABI specifications.  
20 These are combined with Angular Distribution Models (ADMs), which are a synergy of ADMs from the  
21 Clouds and the Earth's Radiant Energy System (CERES) and from simulations. Surface condition at the  
22 scale of the ABI products as needed to compute the TOA radiative fluxes come from the International  
23 Geosphere-Biosphere Programme (IGBP). Land classification at 1/6 ° resolution for 18 surface types are  
24 converted to the ABI 2-km grid over the (CONtiguous States of the United States) (CONUS) and  
25 subsequently re-grouped to 12 IGBP types to match the classification of the CERES ADMs. In the  
26 simulations, default information on aerosols and clouds is based on the ones used in MODTRAN.

27 Comparison of derived fluxes at the TOA is made with those from CERES and the level of agreement  
28 for both clear and cloudy conditions is documented. Possible reasons for differences are discussed. The  
29 product is archived and can be downloaded from the NOAA Comprehensive Large Array-data  
30 Stewardship System (CLASS).

31

## 32 **Introduction**

33

34 One of the objectives at NOAA/STAR in respect to the utilization of observations from the Advanced  
35 Baseline Imager (ABI) is to be able to derive shortwave ( $SW\downarrow$ ) radiative fluxes at the surface. To get to  
36 the surface  $SW\downarrow$  from TOA satellite observations, there are two generic approaches: 1) the direct approach  
37 and 2) the indirect approach. In the direct approach one uses all the necessary information needed for  
38 deriving the surface fluxes (some of which can be derived from satellites). Implementation of such an  
39 approach is feasible, for instance, with observations from MODIS which has a long history of product  
40 availability and evaluation. Examples are illustrated in Wang and Pinker (2009), Niu and Pinker, (2015),  
41 Ma et al. (2016), Pinker et al. (2018), Pinker et al., (2017a), Pinker et al. (2017b). GOES-R is a new  
42 instrument and as yet, similar information to the one from MODIS is not available. Therefore, the indirect  
43 approach is used where one starts from satellite observations at the TOA and models the atmosphere and  
44 surface with best available information (which does not have to be based on ABI). Examples of such an  
45 approach are discussed in Pinker, Zhang and Dutton (2005), Ma and Pinker (2012) and Zhang et al.  
46 (2019). The “indirect path method” is used at the Center for Satellite Applications and Research (STAR)  
47 (Laszlo et al., 2020) for deriving  $SW\downarrow$  radiative fluxes from satellite observations; it requires knowledge  
48 of the SW broadband (0.2 – 4.0  $\mu\text{m}$ ) top of the atmosphere (TOA) albedo. The Advanced Baseline Imager  
49 (ABI) observations onboard of the NOAA GOES-R series of satellites provide reflectance in six narrow  
50 bands in the shortwave spectrum (**Table 1**); these must be first transformed into broadband reflectance  
51 (the NTB conversion), and the broadband reflectance must be transformed into a broadband albedo (the  
52 ADM conversion). During the pre-launch activity NTB transformations were developed based on  
53 theoretical radiative transfer simulations with MODTRAN-3.7 and 14 land use classifications from the

54 International Geosphere-Biosphere Programme (*IGBP*) (Hansen et al., 2010). They were augmented with  
55 ADMs from (CERES) observed ADMs (Loeb et al., 2003) and theoretical simulations (Niu and Pinker,  
56 2011) to compute TOA fluxes. The resulting NTB transformations and ADMs have been tested using  
57 proxy data and simulated ABI data. The proxy instruments used in these early simulations include the  
58 GOES-8 satellite, the Advanced Very-High Resolution Radiometer (AVHRR) sensor on the Polar  
59 Orbiting satellites, the Spinning Enhanced Visible Infra-Red Imager (SEVIRI) sensor on the European  
60 METEOSAT Second Generation (MSG) satellites, and the Moderate Resolution Imaging  
61 Spectroradiometer (MODIS) instrument on the NASA Terra and Aqua Polar Orbiting satellites (Pinker  
62 et al., 2021, unpublished). For each of these satellites, the evaluation of the methodologies was done  
63 differently; some results were evaluated against ground observations while others, against TOA  
64 information from CERES as well as from the (ESA) Geostationary Earth Radiation Budget (GERB)  
65 satellite (Harries et al., 2005). The results obtained provided an insight on the expected performance of  
66 the new ABI sensor. Those procedures have been subsequently updated and applied to the new ABI  
67 instrument once it was built and fully characterized.

68 [This is a first paper that describes the development of a methodology to derive TOA SW fluxes from the](#)  
69 [Advanced Baseline Imager onboard the NOAA GOES-R series of geostationary satellites that are used at](#)  
70 [NOAA STAR as a starting point for deriving surface SW<sub>↓</sub> fluxes. Evaluation of the methodology against](#)  
71 [best available estimates of TOA fluxes was also done. The TOA reflected SW flux is produced at NOAA](#)  
72 [together with the surface SW<sub>↓</sub> flux and is archived at the NOAA Comprehensive Large Array-data](#)  
73 [Stewardship System \(CLASS\) at \[avl.class.noaa.gov\]\(http://avl.class.noaa.gov\). While the TOA reflected SW flux is a product on its](#)  
74 [own right, it is also a prerequisite to deriving the SW<sub>↓</sub> surface flux; as such, versions for TOA and surface](#)  
75 [have the same labeling.](#) The methodology will be presented in section 2, data used are described in section  
76 3, results in section 4 and a summary and discussion in section 5.

77  
78  
79  
80

**Deleted:**

**Formatted:** Tab stops: Not at 0.69"

**Formatted:** Font: (Default) +Headings CS (Times New Roman), 12 pt

**Deleted:** SW

**Formatted:** Font: (Default) +Headings CS (Times New Roman), 12 pt

**Deleted:** To find out how the methodology is working

**Deleted:** e

**Formatted:** Font: (Default) +Headings CS (Times New Roman), 12 pt

**Deleted:** downward SW

**Formatted:** Font: (Default) +Headings CS (Times New Roman), 12 pt

**Deleted:** SW

**Formatted:** Font: (Default) +Headings CS (Times New Roman), 12 pt

**Deleted:** ¶

¶  
¶  
¶

**Deleted:** In this paper we describe activity in support of effort to derive surface shortwave (SW<sub>↓</sub>) radiative fluxes from the operational Advanced Baseline Imager (ABI) instrument on the GOES-R series of the NOAA geostationary meteorological satellites using the latest version of the ABI data. We describe the physical basis of the development of the (NTB) transformations of satellite observed radiances and the bi-directional corrections to be applied to the broadband reflectance to obtain broadband TOA albedo.

## 2. Methodology

The following two flowcharts (Figs. 1 and 2) describe the necessary steps to derive the NTB transformations and the ADMs. Details on these two steps will follow.

The TOA narrowband and broadband reflectance can be calculated from the spectral radiances simulated from MODTRAN 4.3 and the response functions of the satellite sensor as shown in equations (1) and (2):

$$\rho_{nb}(\theta_0, \theta, \phi) = \frac{\pi \int_{\lambda_1}^{\lambda_2} I(\lambda, \theta_0, \theta, \phi) G(\lambda) d\lambda}{\int_{\lambda_1}^{\lambda_2} \cos(\theta_0) S_0(\lambda) G(\lambda) d\lambda} \quad (1)$$

$$\rho_{bb}(\theta_0, \theta, \phi) = \frac{\pi \int_{0.2\mu m}^{4\mu m} I(\lambda, \theta_0, \theta, \phi) d\lambda}{\int_{0.2\mu m}^{4\mu m} \cos(\theta_0) S_0(\lambda) d\lambda} \quad (2)$$

where  $\rho_{nb}$  is narrowband reflectance;  $\rho_{bb}$  is broadband reflectance;  $\theta_0$ : solar zenith angle;  $\theta$ : view (satellite) zenith angle;  $\phi$ : relative azimuth angle;

$I_\lambda$ : reflected spectral radiance;  $S_0(\lambda)$ : solar spectral irradiance;

$G_\lambda$ : spectral response functions of satellite sensors;  $\lambda_1$  and  $\lambda_2$  are the spectral limits of the sensor spectral band. This approach is widely used in the scientific community as also implemented in the work of Loeb et al (2005), Wielicki et al. (2008), Su et al. (2015) and Akkermans et al. (2020).

As stated previously, the ADMs from CERES-based observations (Loeb et al., 2005; Kato et al. 2015) were augmented with theoretical simulations (Niu and Pinker, 2011) to compute TOA fluxes. This was done since CERES observations at that time were under-sampled at higher latitudes.

120 The combined ADMs are developed for each angular bin by weighting the modeled and CERES ADMs  
121 based on the number of samples used to derive the ADMs of each type (Niu et al., 2011). Specifically:

$$122 \quad \bar{R}(\theta_0, \theta, \phi) = \frac{1}{m+n} (m \times R_{CERES}(\theta_0, \theta, \phi) + n \times R_S(\theta_0, \theta, \phi)) \quad (3)$$

123  $\bar{R}(\theta_0, \theta, \phi)$ : averaged ADMs at each angular bin;

124  $R_{CERES}$ : anisotropic factor from CERES ADMs;

125  $R_S$ : anisotropic factor from simulated ADMs;

126  $m$  and  $n$ : observation numbers at angular bins for CERES and simulated ADMs.

## 127

### 128 **2.1 Selection of Atmospheric profiles for simulations**

129

130 We have selected 100 atmospheric profiles covering the globe and the seasons as input for simulations  
131 with MODTRAN4.3. The atmospheric profiles at each pressure level include temperature, water vapor  
132 and ozone. Each season includes 25 profiles. A tool was developed to select profiles from a Training Data  
133 set known as SeeBor Version 5.0 ([https://cimss.ssec.wisc.edu/training\\_data/](https://cimss.ssec.wisc.edu/training_data/)) (Borbas et.al. 2005).  
134 Originally it consisted of 15704 global profiles of temperature, moisture, and ozone at 101 pressure levels  
135 for clear sky conditions. The profiles are taken from NOAA-88, and the European Centre for Medium-  
136 Range Weather Forecasts (ECMWF) 60L training set, TIGR-3, ozone-sondes from 8 NOAA Climate  
137 Monitoring and Diagnostics Laboratory (CMDL) sites, and radiosondes from the Sahara Desert during  
138 2004. A technique to extend the temperature, moisture, and ozone profiles above the level of existing data  
139 was also implemented by the providers (University of Wisconsin-Madison, Space Science and  
140 Engineering Center, Cooperative Institute for Meteorological Satellite Studies (CIMSS)). **Fig. 3** shows the  
141 location of the selected profiles.

142 The SeeBor profiles are clear sky profiles. The top of the profiles is at 0.005 mb which is about 82.6 km.  
143 We did an experiment to check the impact of reducing the number of levels for a profile (initially, we  
144 have used only 40 levels). In the experiment computed were radiances from profiles with 50 levels as  
145 well as radiances from profiles with 98 Levels. The difference between the two radiances (50 lev-98 lev)  
146 were below 5 % reaching 15 % around 2.5  $\mu\text{m}$ . In the experiment we used the odd number levels starting  
147 from surface (plus the highest level) to reduce the number of profile levels. Based on these experiments  
148 we have opted to keep all 98 profile levels.

149 The surface variables we have used are from MODIS and include surface skin temperature, 2 m  
150 temperature, land/sea mask, and albedo. We have conducted a thorough investigation how the selected  
151 profiles represent the entire sample of 15704 profiles. An example showing the comparison of  
152 temperature, humidity and ozone profiles is shown in **Fig. 4**. As seen, there is a positive bias in the selected  
153 profile of temperature due to their higher concentration at the lower latitudes. A positive bias can be found  
154 at the lower levels while a negative bias is seen above 1 mb. Since our domain of study is in such latitudes  
155 this selection should not have adverse effects on the simulations performed.

156

## 157 **2.2 Surface conditions**

158

159 Surface condition is one of the primary inputs into the MODTRAN simulations. The International  
160 Geosphere-Biosphere Programme (IGBP) land classification is used as a source (Hansen et al., 2010;  
161 Loveland et al., 2010). The dataset is at 1/6-degree resolution and includes 18 surface types. We have  
162 converted the 1/6° (~18.5 km) resolution to the ABI 2-km grid using the nearest grid method (**Fig. 5**). The  
163 surface type is fixed in time. The method for cloudy sky uses 4 surface types; these are also derived from  
164 12 IGBP types (**Table 2**).

165

166

167

168

### 2.3 Clear and cloudy sky simulations

Under clear sky, scattering from aerosols is important. We have included 6 aerosol types (**Table 3**) to cover a range of possible conditions under clear sky. Aerosol models are selected based on the type of extinction and a default meteorological range for the boundary-layer aerosol models as listed below:

Aerosol Type 1: Rural extinction, visibility = 23 km

Aerosol Type 4: Maritime extinction, visibility = 23 km

Aerosol Type 5: Urban extinction, visibility = 5 km

Aerosol Type 6: Tropospheric extinction, visibility = 50 km

Aerosol Type 8: Advective Fog extinction, visibility = 0.2 km

Aerosol Type 10: Desert extinction for default wind conditions

For the 6 aerosol types, the total number of MODTRAN simulations for each surface type is 462,000. It is obtained as follows: 6 aerosol types x 100 profiles x 770 angles.

When performing NTB simulations, we use all 6 types of aerosols. The Rural, Ocean, Urban and Fog aerosols are distributed in the lower 0-2 km region. Tropospheric aerosol is distributed from 0 to 10 km tropopause. The Rural, Ocean, Urban and Tropospheric aerosol optical properties have Relative Humidity (RH) dependency. The Single Scattering Albedo (SSA) is given on 4 RH grids (0, 70, 80, 99) on a spectral grid of 788 points ranging from 0.2 to 300 microns.

Simulations were performed for ABI for all the cloud cases described in **Table 3**. To merge cloud layers with atmospheric profiles we have followed the procedure as described in *Berk et al.* (1985, 1998), namely: "Cloud profiles are merged with the other atmospheric profiles (pressure, temperature, molecular constituent, and aerosol) by combining and/or adding new layer boundaries. Any cloud layer boundary within half a meter of an atmospheric boundary layer is translated to make the layer altitudes coincide; new atmospheric layer boundaries are defined to accommodate the additional cloud layer boundaries." 100% relative humidity is assumed within the cloud layers (default).

196 **2.4 Selection of angles**

197  
198 The total number of angles used in the simulations is given in **Table 4**. The selected spectral grids for  
199 solar zenith angles, satellite view angles and relative azimuth angles are at Gaussian quadrature points,  
200 plus 0° to solar zenith angles (sza) and satellite viewing angles (vza) and 0° and 180° (forward and  
201 backward view) to the satellite relative azimuth angles. Solar angle and satellite view angle are referenced  
202 to target or surface for satellite simulation with 0° meaning looking up (zenith). Relative azimuth angle is  
203 defined as when the relative azimuth angle equals 180°, the sun is in front of observer.

204 The definitions of solar zenith angle and azimuth angle in this table corresponds to the definitions of  
205 MODTRAN but that is not the case for the satellite zenith angle. MODTRAN uses nadir angle as 180°-  
206 satellite zenith angle, ignoring spherical geometry.

207  
208 **2.5 Selection of optimal computational scheme**

209  
210 MODTRAN4.3 provides three multiple scattering models (Isaacs, DISORT, and Scaled Isaacs) and three  
211 band models at resolutions (1 cm<sup>-1</sup>, 5 cm<sup>-1</sup>, and 15 cm<sup>-1</sup>). The DISORT model (Stamnes et al., 1988)  
212 provides the most accurate radiance simulations but the runs are very time consuming. The Isaacs (Isaacs  
213 et al. 1987) 2-stream algorithm is fast but oversimplified. The Scaled Isaacs method performs radiance  
214 calculations using Isaacs 2-stream model over full spectral range and using DISORT model at a small  
215 number of atmospheric window wavelengths. The multiple scattering contributions for each method are  
216 identified and ratios of the DISORT and Isaacs methods are computed. This ratio is interpolated over the  
217 full wavelength range, and finally, applied as a multiple scattering scale factor in a spectral radiance  
218 calculation performed with the Isaacs method.

219 To optimize simulation speed and accuracy, we performed various sensitivity tests, including  
220 combinations of multiple scattering models, band resolution, and number of streams. **Table 5** lists  
221 simulation options and their corresponding calculation speed.



222 Based on results presented in **Table 5**, the efficient options (< 40 seconds) are Isaacs, DISORT 2-stream  
223 with  $15\text{ cm}^{-1}$ , DISORT 4-stream  $15\text{ cm}^{-1}$ , and Scaled Isaacs all streams at all resolutions. Although the  
224 ideal option is DISORT 8-stream with  $1\text{ cm}^{-1}$  resolution, there is a trade-off between speed and accuracy.  
225 **Fig. 6** compares DISORT simulated radiances at three band resolutions. We use two spectral ranges of  
226  $0.4 - 0.5\ \mu\text{m}$  and  $1.5 - 2.0\ \mu\text{m}$  to illustrate differences. **Fig. 6** shows that the coarser band resolution has  
227 smoothed out the radiance variations. The  $15\text{ cm}^{-1}$  has the smoothest curve among the three, and  $1\text{ cm}^{-1}$   
228 shows more variations than the other two. Another (scientific) criteria for selecting the spectral resolution  
229 is the ability to resolve/match the relative spectral response function (SRF) of a sensor. For example, the  
230 SRFs of channels 1-6 of ABI are given at every  $1\text{ cm}^{-1}$ .

231 Accordingly, we have chosen the  $1\text{ cm}^{-1}$  band model for the MODTRAN radiance simulations. Performed  
232 were also radiance simulations from different multiple scattering models at  $1\text{ cm}^{-1}$  resolution. The whole  
233 spectrum of  $0.2 - 4\ \mu\text{m}$  was separated to 14 sections so that the differences can be assessed clearly. For  
234 wavelength below  $0.3\ \mu\text{m}$  and beyond  $2.5\ \mu\text{m}$  no discernible differences were found among Isaacs, DISORT  
235 2-, 4-, and 8-stream, and Scaled Isaac. The largest differences occurred in the spectral range of  $0.4 - 1.0$   
236  $\mu\text{m}$ . Scaled Isaac 8-stream follows DISORT 8-stream closely across the whole spectral range; the Scaled  
237 Isaac method provided near-DISORT accuracy with the speed of Isaacs. Thus, the MODTRAN4.3  
238 simulations for GOES-R ABI were set-up with Scaled Isaac 8-stream with  $1\text{ cm}^{-1}$  band resolution.

239 For illustration, in **Fig. 7** compared are radiances simulated by Isaac 2 stream, Scaled Isaac, and DISORT-  
240 4 stream for the case of Relative Azimuthal Angle= $1.9^\circ$ , View Angle= $76.3^\circ$ , Solar Zenith Angle= $87.2^\circ$ .  
241 The lines are differences between various settings and DISORT-8 stream (e.g. Isaacs minus DISORT-8).  
242 Isaac has the least accuracy since it is oversimplified, 4-stream showed some improvements when  
243 compared with Isaac while still has large differences for  $0.4\ \mu\text{m}$  and is still computationally demanding.  
244 Scaled Isaac provides the smallest differences between DISORT-8. **Fig. 7** (lower) zoomed in to the large  
245 difference area of  $0.3-0.35\ \mu\text{m}$  which indicates that Scaled Isaacs still provides satisfactory results.

246  
247  
248

## 2.6 Regression methodologies

We have derived coefficients of regression using a constrained least-square curve fitting methods of Matlab, “lsqnonneg”, which can solve a linear or nonlinear least-squares (data-fitting) problem and produce non-negative coefficients. Non-negative coefficients avoid generating negative TOA flux, which is not a physically valid.

To ensure that information from all channels is used and avoid the complex cross-correlation problem, it was opted to generate Narrow to Broad (NTB) coefficients for each ABI channel separately. These channel specific NTB coefficients are applied to each channel to convert ABI narrow-band reflectance to extended band. The final broad-band TOA reflectance is taken as the weighted sum of all 6-channel specific broad-band reflectance. The logic behind this approach is the assumption that the narrow-band reflectance from each channel is a good representative for a limited spectral region centered around the channel and the total spectral reflectance is dominated by the spectral region that contains the most solar energy.

To generate “separate-channel” NTB coefficients, each narrow-band ABI channel reflectance is converted to a reflectance  $\rho_{bb,i}$  separately,

$$\rho_{bb,i}(\theta_0, \theta, \phi) = c_{0,i}(\theta_0, \theta, \phi) + c_{1,i}(\theta_0, \theta, \phi) * \rho_{nb,i}(\theta_0, \theta, \phi) \quad (4)$$

where  $\rho_{bb,i}$  is the band reflectance for an interval around each channel  $i$ ;  $c_{0,i}$  and  $c_{1,i}$  are regression coefficients for channel  $i$ . These regression coefficients are derived separately for various combination of surface, cloud and aerosol types. The total shortwave broad band (0.25 – 4.0 $\mu\text{m}$ ) reflectance  $\rho_{bb}^{est}$  is obtained by taking the weighted sum of all 6  $\rho_{bb,i}$  reflectance

$$\rho_{bb}^{est}(\theta_0, \theta, \phi) = \sum_i \rho_{bb,i}(\theta_0, \theta, \phi) \frac{S_{0,i}}{S_0} \quad (5)$$

Here,  $S_0$  and  $S_{0,i}$  are total solar irradiance and band solar irradiance for each channel, respectively. Band edges around the six ABI channels are: 49980-18723, 18723-13185, 13185-9221, 9221-6812, 6812-5292, 2500  $\text{cm}^{-1}$  0.2001-0.5341, 0.5341-0.7584, 0.7584-1.0845, 1.0845-1.4680, 1.4680-1.8896, 1.8896-4.0000  $\mu\text{m}$ ). The corresponding solar irradiance band values are 364, 360, 287, 168, 91, 87

275  $W m^{-2}$ . **Fig. 8** shows the sensor response function (SRF) and locations of the six ABI channels.  
276 Coefficients are generated for clear condition and 3 types of cloudy conditions. Comparison between ABI  
277 TOA flux and CERES products are shown in **Fig. 9**. The “separate-channel” coefficients work well for  
278 predominantly clear sky (**Fig.10**). Differences are somewhat more scattered for cloudy cases. The reason  
279 may be due to the fact that the ABI observation time and CERES product time do not match perfectly  
280 since cloud condition change quickly. As discussed in Gristey et al. (2019) there are SW spectral  
281 reflectance variations for different cloud types. Possibly, for ABI bands some spectral variations  
282 associated with cloud variability are missed. It is important to have the correct cloud properties to be able  
283 to select correct ADM. Misclassification of cloud properties will therefore result in flux differences. They  
284 also argue that ADMs have an uncertainty due to within-scene variability and within-angular bin  
285 variability leading to additional flux differences.

### 287 3. Data used

#### 289 3.1 Satellite data for GOES-16 and GOES-17

291 The Advanced Baseline Imager (ABI) data used (Table 6) were downloaded from the NOAA  
292 Comprehensive Large Array-Data Stewardship System (CLASS) at  
293 <https://www.avl.class.noaa.gov/saa/products/welcome>. Both level 1b (L1b) and level 2 (L2) data were  
294 used. These can be found by searching the CLASS site by selecting "GOES-R Series ABI Products  
295 GRABIPRD (partially restricted L1b and L2+ Data Products)". The L1b data included the radiances  
296 (RadC) in files "OR ABI-L1b-RadC-MmCnn G1SS stime etime ctime, where "m", "nn" and "SS"  
297 indicate the ABI scan mode, channel number (01-06) and satellite identification number (16 or 17),  
298 respectively. "stime", and "etime" are the start and end dates and times of the scan, "ctime" is the date  
299 and time the file was created. The ABI L2 product used were the clear-sky mask, cloud top phase, cloud  
300 optical depth. The names of these files are constructed similarly to the L1b radiance files, except that the  
301 radiance product name RadC is replaced by APMC, ACTPC, CODC and AODC, respectively, and the

**Deleted:** The GOES Imager data used (**Table 6**) were downloaded from <https://www.avl.class.noaa.gov/saa/products/welcome>.

**Formatted:** Font: (Default) +Headings CS (Times New Roman), 12 pt

**Deleted:**

**Formatted:** Font: (Default) +Headings CS (Times New Roman), 12 pt

**Formatted:** Font: (Default) +Headings CS (Times New Roman), 12 pt

**Formatted:** Font: (Default) +Headings CS (Times New Roman), 12 pt

**Deleted:** on

**Formatted:** Font: (Default) +Headings CS (Times New Roman), 12 pt

307 [reference to the channel number is omitted. For example, GOES-16 with ABI operating in scan mode 6](#)  
308 [in the CONUS domain, the name of the clear-sky mask file is OR\\_ABI-L2-ACMC-M6\\_G16\\_](#)  
309 [stime etime ctime. \(In the product names above the letter C indicates the CONUS domain.\)](#)  
310 [The clear-sky mask product consists of a binary cloud mask identifying pixels as clear, probably clear,](#)  
311 [cloudy or probably cloudy. The cloud top phase product provides cloud classification identification](#)  
312 [information for each pixel. The cloud phase categories are clear sky, liquid water, super cooled liquid](#)  
313 [water, mixed phase, ice, and unknown. The cloud optical depth product gives the optical thickness along](#)  
314 [an atmospheric column for each pixel. All products have a nominal sub-satellite spatial resolution of 2](#)  
315 [km.](#)

316 When searching the NOAA CLASS site, go to "GOES-R Series ABI Products GRABIPRD (partially  
317 restricted L1b and L2+ Data Products)". The SRF are downloaded from  
318 <https://ncc.nesdis.noaa.gov/GOESR/ABI.php>.

### 319 **3.2 Reference data from CERES**

320

321

322 The CERES Single Scanner Footprint (SSF) is a unique product for studying the role of clouds, aerosols,  
323 and radiation in climate. Each CERES footprint (nadir resolution 20-km equivalent diameter) on the SSF  
324 includes reflected shortwave (SW), emitted longwave (LW) and window (WN) radiances and top-of-  
325 atmosphere (TOA) fluxes from CERES with temporally and spatially coincident imager-based radiances,  
326 cloud properties, and aerosols, and meteorological information from a fixed 4-dimensional analysis  
327 provided by the Global Modeling and Assimilation Office (GMAO). Each file in this data product  
328 contains one hour of full and partial-Earth view measurements or footprints at a surface reference level.  
329 Detailed information can be found via <https://ceres.larc.nasa.gov/data/#ssf-level-2> (we used version 4a)  
330 Near real-time CERES fluxes and clouds in the SSF format are available within about a week of  
331 observation (Kratz et al., 2014). They do not use the most recent CERES instrument calibration and thus  
332 contains some uncertainty. Before GOES data were transferred to the Comprehensive Large Array-data

**Formatted:** Font: (Default) +Headings CS (Times New Roman)

**Formatted:** Font: (Default) +Headings CS (Times New Roman), 12 pt

**Formatted:** Justified, Line spacing: 1.5 lines

333 Stewardship System (CLASS) system, the NOAA/STAR archive was holding new data for about a week.  
334 Therefore, the initial evaluations had to be done only with data that overlapped in time. The CERES data  
335 known as the FLASHFlux Level2 (FLASH\_SSF) are available almost in real time from:  
336 <https://ceres.larc.nasa.gov/products.php?product=FLASHFlux-Level2> (we used version 3c).  
337 Due to such constraints the early comparison was done between ABI data as archived at NOAA/STAR  
338 and the FLASHFlux products (in this paper, the FLASHFlux data were used only in Fig. 9). The archiving  
339 of GOES-R at the NOAA Comprehensive Large Array-data Stewardship System (CLASS) started only  
340 in 2019, however, it contains data starting from 2017. Once the CLASS archive became available, we  
341 have augmented GOES-16 cases with observations from GOES-17; only those cases will be shown in this  
342 paper.

343

### 344 **3.3 Data preparation**

345

346 For the re-mapping, we adopted the ESMF re-gridding package. The detailed information can be found  
347 at: <http://earthsystemmodeling.org/regrid/>

348 For an ideal situation, the ABI high-resolution TOA SW fluxes should be mapped into the CERES  
349 footprint for validation. However, there are reasons that make it difficult to do so. There can be more than  
350 18000 pixels in a single swath of the SSF, when constrained to U.S. Different pixels have different times.  
351 Neglecting the seconds, there are still more than 30 mins differences (this changes case by case) between  
352 the first pixel and the one at the end and this brings up a time matching issue. By remapping the SSF to

353 ABI, we can set up a unique time for ABI (ABI is at 5 min intervals) and then constrain the region and  
354 the time range of SSF.

355 Both re-mapping the ABI to SSF and remapping SSF to the ABI bring up spatial matching errors as  
356 recognized by the scientific community (Rilee and Kuo, 2018; Ragulapati et al., 2021). In **Fig. 11**, we  
357 show the SSF before re-gridding (**Figs 11 (a) & (b)**) and after re-gridding (**Figs. 11 (c) and (d)**). The  
358 fluxes after re-mapping CERES SSF to the ABI resolution resemble well the original structure. Another  
359 consideration is the computational efficiency of re-mapping the curvilinear tripolar grid to unconstructed  
360 grid. For large arrays, it is more efficient to remap the unconstructed grid to the curvilinear tripolar grid.

361

## 362 **4. Results**

363

### 364 **4.1 Comparison between ABI TOA fluxes to those from CERES SSF**

365 A case for 2019/12/26 (doy 360) UTC 19:36 is illustrated in **Figs. 11-14**. Statistical summaries from an  
366 extended number of cases that cover all four seasons are presented in **Table 7**.

367 We have conducted several experiments to select an appropriate regression approach to the NTB  
368 transformation ensuring that non-physical results are not encountered. Based on the samples used in this  
369 study (**Table 7**) the differences found for Terra and GOES-16 were in the range of -0.5-(-17.37) for bias  
370 and 43.28-81.72 for standard deviation; for Terra and GOES-17 they were 11.26-47.09 and 70.25-108.73,  
371 respectively. For Aqua and GOES-16 they were 7.63-33.87 and 58.68-117.43 respectively while for Aqua  
372 and GOES-17 they were 0.19-31.53 and 47.55-129.42, respectively (all units are  $W m^{-2}$ ). The evaluation  
373 process revealed the challenges in undertaking such comparisons. Both estimates of TOA fluxes (CERES  
374 and GOES) do no account for seasonality in the land use classification; the time matching for the different  
375 satellites is important and limits the number of samples that can be used in the comparison. Based on the  
376 results of this study recommendation for future work include the need to incorporate seasonality in land

377 use and spectral characteristic of the various surface types. Possible stratification by season in the  
378 regressions could also be explored.

## 380 **4.2 Causes for differences between ABI and CERES TOA fluxes**

### 382 **4.2.1 Differences in surface spectral reflectance**

383  
384 In the MODTRAN simulations we use the spectral reflectance information on various surface types as  
385 provided by MODTRAN. MODTRAN version 4.3.1 contains a collection of spectral surface reflectance  
386 dataset from the Moderate Spectral Atmospheric Radiance and Transmittance (MOSART) model  
387 (Cornette et al., 1994) and others from Johns Hopkins University Spectral Library (Baldrige et al., 2009).  
388 When doing simulation, we call the built-in surface types and use the provided surface reflectance. As  
389 such, the spectral dependence of the surface reflectance used in the simulations and matched to the  
390 CERES surface types may not be compatible with the classification of CERES. Also, seasonal changes  
391 in surface type classification can introduce errors due to changes in the spectral surface reflectance for  
392 different surface types (**Fig. 15**).

### 394 **4.2.2 Issues related to surface classification**

395  
396 Another possible cause for differences between the TOA fluxes is the classification of surface types as  
397 originally identified by the IGBP and used in the simulations. No seasonality is incorporated in the surface  
398 type classification while such variability is part of the CERES observations.

### 400 **4.2.3 Issues related to match-up between GOES-R and CERES**

401  
402 Both Terra and Aqua have sun-synchronous, near-polar circular orbits. Terra is timed to cross the equator  
403 from north to south (descending node) at approximately 10:30 am local time. Aqua is timed to cross the

404 equator from south to north (ascending node) at approximately 1:30 pm local time. The periods for Terra  
405 and Aqua are 99 and 98 minutes, respectively. Both have 16 orbits per day. CERES on Terra and Aqua  
406 optical FOV at nadir is 16 x 32 or 20 km resolution. Terra passes CONUS during 03-06 UTC (US night  
407 time), 16-20 UTC (US day time), and Aqua passes CONUS during 07-11 UTC (US night time), 18-22  
408 UTC (US day time).

409 Both Terra and Aqua have an instantaneous FOV values at SWATH level. There is no perfect overlap,  
410 temporally or spatially with ABI data. The ABI radiance and cloud data are on a regular grid of 2\*2 km  
411 over CONUS at each hour. To use CERES data for evaluation of ABI, there is a need to perform  
412 collocation in both time and space.

## 414 **5. Summary**

415  
416 The derivation and evaluation of TOA radiative fluxes as simulated for any given instrument are quite  
417 challenging. In principle, there is a need to account for all possible changes in the atmospheric and surface  
418 conditions one may encounter in the future. Yet, to know what these conditions are at the time of actual  
419 observation when there is a need to select the appropriate combination of variables from the simulations,  
420 is a formidable task. Differences in assumed cloud properties can also lead to differences in the fluxes  
421 derived from the two instruments. Therefore, error can be expected due to discrepancies between the  
422 actual conditions and the selected simulations and these are difficult to estimate. The approach we have  
423 selected is based on high-quality simulations using a proven and accepted radiative transfer code  
424 (MODTRAN) of known configurations and a wide range of atmospheric conditions. We have also  
425 selected the best available estimates of TOA radiative fluxes from independent sources for evaluation.  
426 However, the matching between different satellites in space and time is challenging. In selecting the cases  
427 for evaluation, we have adhered to strict criteria of time and space coincidence as described in section  
428 3.3.

429 Critical elements of an inference scheme for TOA radiative flux estimates from satellite observations are:  
430 1) transformation of narrowband quantities into broadband ones;



431 2) transformation of bi-directional reflectance into albedo by applying Angular Distribution Models  
432 (ADMs). In principle, the order in which these transformations are executed is arbitrary. However, since  
433 well established, observation-based broadband ADMs derived from the Clouds and the Earth's Radiant  
434 Energy System (CERES) project already exist, the logical procedure is to do the NTB transformation on  
435 the radiances first, and then apply the ADM. This is the sequence that has been followed here. While the  
436 road map to accomplish above objectives seems well defined, reaching the final goal of having a stable  
437 up-to-date procedure for deriving TOA radiative fluxes from a new instrument like the ABI on the new  
438 generation of GOES satellites is quite complicated. Since the final configuration of the instrument  
439 becomes known at a much later stages the evaluation of new algorithms is in a fluid stage for a long time  
440 so early evaluation against "ground truth" needs to be repeated frequently. Additional complication is  
441 related to the lack of maturity of basic information needed in the implementation process, such as a  
442 reliable cloud screened product which in itself is in a process of development and modifications. The  
443 "ground truth", namely, the CERES observations are also undergoing adjustments and recalibration. As  
444 such, the process of deriving best possible estimates of TOA radiative fluxes from ABI underwent  
445 numerous iterations to reach its current status. An effort was made to deal the best way possible with the  
446 fluid situation. All the evaluations against CERES were repeated once the ABI data reached stability and  
447 were archived in CLASS and we used the most recent auxiliary information. This study sets the stage for  
448 future possible improvements. One example is land classification which currently is static. Another issue  
449 is related to the representation of real time aerosol optical properties which are important under clear sky  
450 conditions. It is believed that only now when NOAA/STAR has a stable aerosol retrieval algorithm, it  
451 would be timely to address the aerosol issue in the estimation of TOA fluxes under clear sky.

452  
453 Data availability. The data are available upon request from the corresponding author.

454 Author contributions. The investigation and conceptualization were carried out by RTP, IL and JD. YM  
455 and WC developed the software. RTP prepared the original draft. All authors contributed to the writing,  
456 editing and review of the publication.

457 Competing interests. The authors declare that they have no conflict of interest.

458 Disclaimer. Publisher's note: Copernicus Publications remains neutral with regard to jurisdictional claims  
459 in published maps and institutional affiliations.

460 Acknowledgements. We acknowledge the benefit from the use of the numerous data sources used in this  
461 study. These include the Clouds and the Earth's Radiant Energy System (CERES) teams, the Fast  
462 Longwave and Shortwave Radiative Flux (FLASHFlux) teams, the  
463 University of Wisconsin-Madison, Space Science and Engineering Center, Cooperative Institute for  
464 Meteorological Satellite Studies (CIMSS) for providing the SeeBor Version 5.0 data  
465 ([https://cimss.ssec.wisc.edu/training\\_data/](https://cimss.ssec.wisc.edu/training_data/)), and the final versions of the GOES Imager data were  
466 downloaded from <https://www.bou.class.noaa.gov/>. Several individuals have been involved in the early  
467 stages of the project whose contribution led to the refinements of the methodologies. These include M.  
468 M. Wonsick and Shuyan Liu. We thank the anonymous Reviewers for a very thorough and constructive  
469 comments that helped to improve the manuscript. We thank the Editor Sebastian Schmidt for overseeing  
470 the disposition of the manuscript.  
471

472 Financial support. This research was supported by NOAA/NESDIS GOES-R Program under grants  
473 5275562 1RPRP\_DASR and 275562 RPRP\_DASR\_20 to the University of Maryland.

474

475

476 **Reference:**

- 477 Akkermans T., and Clerbaux, N.: Narrowband-to-Broadband Conversions for Top-of-Atmosphere  
478 Reflectance from the Advanced Very High-Resolution Radiometer (AVHRR),  
479 Remote Sens. 12 (2), 305; <https://doi.org/10.3390/rs12020305>, 2020.
- 480 Berk, A., Bernstein, L. W., and Robertson, D. C.: MODTRAN: A moderate resolution model for  
481 LOWTRAN 7, Philips Laboratory, Report AFGL-TR-83-0187, Hanscom AFB, MA, 1985.
- 482 Berk, A., G. P. Anderson, P. K., Acharya, D. C. Robertson, J. H. Chetwynd, S. M. Adler-Golden:  
483 MODTRAN Cloud and Multiple Scattering Upgrades with Application to AVIRIS, Remote Sensing  
484 of Environment, 65 (3), 367-375, [https://doi.org/10.1016/S0034-4257\(98\)00045-5](https://doi.org/10.1016/S0034-4257(98)00045-5), 1998.
- 485 Baldrige, A. M., Hook, S. J., Grove, C. I., Rivera, G.: The ASTER spectral library version 2, Remote  
486 Sensing of Environment 113, doi: 10.1016/j.rse.2008.11.007, 2009.
- 487 Borbas, E. E., Seemann, S. W., Huang, H.-L., Li, J., and Menzel, W. P.: Global profile training database  
488 for satellite regression retrievals with estimates of skin temperature and emissivity. Proceedings of  
489 the XIV, International ATOVS Study Conference, Beijing, China, University of Wisconsin-  
490 Madison, Space Science and Engineering Center, Cooperative Institute for Meteorological Satellite  
491 Studies (CIMSS), Madison, WI, pp.763-770, 2005.
- 492 Clerbaux, N., Russell, J. E., Dewitte, S., Bertrand, C., Caprion, D., De Paepe, B., Sotelino, L. G., Ipe, A.,  
493 Bantges, R., and Brindley, H. E.: Comparison of GERB instantaneous radiance and flux products  
494 with CERES Edition-2 data, Rem. Sens. of Environ., **113**, 102-114. doi:  
495 10.1016/j.rse.2008.08.016, 2009.
- 496 Cornette, W. M., Acharya, P. K., Robertson, D. C., and Anderson, G. P.: Moderate Spectral Atmospheric  
497 Radiance and Transmittance Code (*MOSART*), Rep. R-057-94 (11–30), La Jolla, CA: Photon  
498 Research Associates, 1994.
- 499 Gristey, J. J., Su, W., Loeb, N. G., Vonder Haar, T. H., Tornow, F., Schmidt, K. S., Hakuba, M. Z.,

500 Pilewskie, P., Russell, J. E.: Shortwave Radiance to Irradiance Conversion for Earth Radiation  
501 Budget Satellite Observations: A Review, *Remote Sens.* 13, 2640,  
502 <https://doi.org/10.3390/rs13132640>, 2021.

503 Kato, S., Loeb, N. G., Rutan, D. A., Rose, F. G.: Clouds and the Earth's Radiant Energy System  
504 (CERES) Data Products for Climate Research *Journal of the Meteorological Society of Japan*,  
505 93 (6), 597–612, DOI:10.2151/jmsj.2015-048, 2015.

506 Kratz, D. P., Stackhouse Jr., P. W., Gupta, S. K., Wilber, A. C., Sawaengphokhai, P., and McGarragh, G.  
507 R.: The Fast Longwave and Shortwave Flux (FLASHFlux) Data Product: Single-Scanner Footprint  
508 Fluxes, *J. Appl. Meteor. Climatology*, 53, 1059-1079, doi: 10.1175/JAMC-D-13-061.1, 2014.

509 Hansen, M. C., Defries, R. S., Townshend, J. R. G., and Sohlberg, R.: Global land cover classification  
510 at 1km spatial resolution using a classification tree approach, *International Journal of Remote*  
511 *Sensing*, 21(6-7):1331 – 1364, DOI:10.1080/014311600210209  
512 <https://doi.org/10.1080/014311600210209>, 2010.

513 Harries, J. E., Russell, J. E., Hanafin, J. A., Brindley, H., Futyán, J., Rufus, J., Kellock, S., G. Matthews,  
514 R. Wrigley, A. Last, J. Mueller, R. Mossavati, J. Ashmall, E. Sawyer, D. Parker, M. Caldwell, P  
515 M. Allan, A. Smith, M. J. Bates, B. Coan, B. C. Stewart, D. R. Lepine, L. A. Cornwall, D. R.  
516 Corney, M. J. Ricketts, D. Drummond, D. Smart, R. Cutler, S. Dewitte, N. Clerbaux, L. Gonzalez,  
517 A. Ipe, C. Bertrand, A. Joukoff, D. Crommelynck, N. Nelms, D. T. Llewellyn-Jones, G. Butcher,  
518 G. L. Smith, Z. P. Szewczyk, P. E. Mlynyczak, A. Slingo, R. P. Allan, and M. A. Ringer: The  
519 Geostationary Earth Radiation Budget Project, *Bull. Amer. Meteor. Soc.* 86 (7): 945, doi:  
520 10.1175/BAMS-86-7-945, 2005.

521 Isaacs, R. G., W.-C. Wang, R. D. Worsham, and S. Goldenberg, S.: Multiple scattering LOWTRAN and  
522 FASCODE models. *Applied Optics*, 26(7), 1272 – 1281, 1987.

523 Kato, S., and Loeb, N. G.: Top-of-atmosphere shortwave broadband observed radiance  
524 and estimated irradiance over polar regions from Clouds and the Earth's Radiant Energy System  
525 (CERES) instruments on Terra, *J. Geophys. Res.*, 110, D07202,  
526 doi:10.1029/2004JD005308, 2005.

527 Laszlo, I., Liu, H., Kim, H.-Y., and Pinker, R. T. : GOES-R Advanced Baseline Imager (ABI) Algorithm  
528 Theoretical Basis Document (ATBD) for Downward Shortwave Radiation (Surface), and Reflected  
529 Shortwave Radiation (TOA), version 3.1, Available at <https://www.goes-r.gov/resources/docs.html>,  
530 2018.

531 Laszlo, I., Liu, H., Kim, H.-Y., and Pinker, R. T.: Shortwave Radiation from ABI on the GOES-R Series,  
532 in: *The GOES-R Series*, edited by S. J. Goodman, T. J. Schmit, J. Daniels and R. J. Redmon. 179-191,  
533 Elsevier, doi: <https://doi.org/10.1016/B978-0-12-814327-8.00015-9>, 2020.

534 Loeb, N. G., Smith, N. M., Kato, S., Miller, W. F., Gupta, S. K., Minnis, P. and Wielicki, B. A.: Angular  
535 Distribution Models for Top-of Atmosphere Radiative Flux Estimation from the Mission Satellite,  
536 Part I: Methodology, *Journal of Applied Meteorology*, 42 240-265, 2003.

537 Loeb N. G. et al.: Angular distribution models for top-of- atmosphere radiative flux estimation from the  
538 Clouds and the Earth's Radiant Energy System Instrument on the Terra satellite. part I:  
539 Methodology. *J. Atmos. Oceanic Technol.*, 22:338–351, 2005.

540 Loveland T. R., B. C. Reed, J. F. Brown, D. O. Ohlen, Z. Zhu, L. Yang, J. W. Merchant: Development  
541 of a global land cover characteristics database and IGBP DISCover from 1 km AVHRR data,  
542 *International Journal of Remote Sensing*, 21 (6-7), 1303-1330, 2010.

543 Ma, Y., R. T. Pinker, M. M. Wonsick, C. Li, and L. M. Hinkelman: Shortwave radiative fluxes on  
544 slopes. *JAMC*, 55, 1513-1532, <https://doi.org/10.1175/JAMC-D-15-0178.1>, 2016.

545 Ma, Y. and Pinker, R. T.: Shortwave Radiative Fluxes from Satellites: An Update. *J. Geophys. Res.*  
546 *Atmos.*, 117, Issue D23, DOI: 10.1029/2012JD018332, 2012.

547 Niu, X. and Pinker, R. T.: Revisiting satellite radiative flux computations at the top  
548 of the atmosphere, *International Journal of Remote Sensing*, DOI:10.1080/01431161.2011.571298,  
549 2011.

550 Niu, X. and Pinker, R. T.: An improved methodology for deriving high resolution  
551 surface shortwave radiative fluxes from MODIS in the Arctic region, *J. Geophys. Res.*  
552 *Atmos.*, 120, 2382–2393, doi: 10.1002/2014JD022151, 2015.

553 Pinker, R. T., Zhang B., Dutton E. G.: Do satellites detect trends in surface solar radiation? *SCIENCE*,  
554 308, 5723, 850-854, 2005.

555 Pinker, R. T., A. Bentamy, B. Zhang, W. Chen, and Ma, Y.: The net energy budget at the ocean-  
556 atmosphere interface of the “Cold Tongue” region, *J. Geophys. Res. Oceans*, 122, doi: 10.1002/  
557 2016JC012581, 2017a.

558 Pinker, R. T., S. Grodsky, B. Zhang, A. Busalacchi, and Chen, W.: ENSO Impact on Surface Radiative  
559 Fluxes as Observed from Space. *J. Geophys. Res.-Oceans.*, doi: 10.1002/2017JC012900, 2017b.

560 Pinker, R. T., Zhang, B. Z., Weller, R. A., and Chen, W.: Evaluating surface radiation fluxes observed  
561 from satellites in the southeastern Pacific Ocean. *Geophysical Research Letters*, 45.  
562 <https://doi.org/10.1002/2017GL076805>, 2018.

563 Rajulapati, C. R., S. M. Papalexiou, M. P. Clark, and Pomeroy, J. W.: The Perils of Regridding:  
564 Examples Using a Global Precipitation Dataset, *Journal of Applied Meteorology and*  
565 *Climatology*, 60 (11), 1561–1573, doi: 10.1175/JAMC-D-20-0259.1, 2021.

566 Rilee M. L. and Kuo, K. S.: The Impact on Quality and Uncertainty of Regridding Diverse Earth  
567 Science Data for Integrative Analysis, IN43C-0916, 2018.

568 Scarino et al.: A Web-Based Tool for Calculating Spectral Band Difference Adjustment Factors Derived  
569 from SCIAMACHY Hyperspectral Data, *IEEE Trans. Geo. Remote Sens.*, 54, 5,  
570 10.1109/TGRS.2015.2502904, 2016.

571 Stamnes, K., S.-C. Tsay, W. Wiscombe and K. Jayaweera: Numerically stable algorithm for discrete-  
572 ordinate-method radiative transfer in multiple scattering and emitting layered media, *Applied*  
573 *Optics*, 27 (12), 2502–2509, 1988.

574 Su, W., Corbett, J., Eitzen, Z., and Liang, L.: Next-generation angular distribution models for  
575 top-of-atmosphere radiative flux calculation from CERES instruments: methodology, *Atmos.*  
576 *Meas. Tech.*, 8, 611–632, <https://doi.org/10.5194/amt-8-611-2015>, 2015.

577 Wang, H; Pinker, R. T.: Shortwave radiative fluxes from MODIS: Model development and  
578 implementation. *JGR- Atmospheres*, 114, D20201, 2009.

579 Wielicki, B. A.; Doelling, D. R.; Young, D. F.; Loeb, N. G.; Garber, D. P.; MacDonnell, D. G.: Climate  
580 quality broadband and narrowband solar reflected radiance calibration between sensors in orbit.  
581 In Proceedings of the IGARSS 2008 IEEE International Geoscience and Remote Sensing  
582 Symposium, Boston, MA, USA, 7–11 July 2008.

583 Zhang, T., Stackhouse Jr., P. W., Cox, S. J., Mikovitz, J. C., Long, C. N.: Clear-sky shortwave  
584 downward flux at the Earth’s surface: Ground-based data vs. satellite-based data, *Journal of*  
585 *Quantitative Spectroscopy & Radiative Transfer*, 224, 247-260, 2019,  
586 [www.elsevier.com/locate/jqsrt](http://www.elsevier.com/locate/jqsrt).

587  
588  
589  
590

## Tables

Table 1. Channel information and spectral bands for ABI.

<i>ABI Band #</i>	<i>Central wavelength ( <math>\mu m</math> )</i>	<i>Spectral band ( <math>\mu m</math> )</i>
1	VIS 0.47	0.45-0.49
2	VIS 0.64	0.60-0.68
3	NIR 0.86	0.847-0.882
4	NIR 1.38	1.366-1.380
5	NIR 1.61	1.59-1.63
6	NIR 2.26	2.22-2.27

591

592

593



594 Table 2. Surface classification description for IGBP 18 types, IGBP 12 types, CERES clear sky 6 types,  
 595 and NTB cloudy sky 4 types

IGBP (18 types)	IGBP (12 types)	CERES clear-sky (6 types)	NTB cloudy-sky (4 types)
Evergreen Needleleaf	Needleleaf Forest	Mod-High Tree/Shrub	Land
Deciduous Needleleaf			
Evergreen Broadleaf	Broadleaf Forest		
Deciduous Broadleaf			
Mixed Forest	Mixed Forest		
Closed Shrublands	Closed Shrub		
Woody Savannas	Woody Savannas		
Savannas	Savannas	Low-Mod Tree/Shrub	
Grasslands	Grasslands		
Permanent Wetlands			
Tundra			
Croplands	Croplands		
Open Shrublands	Open Shrub		
Urban and Built-up	Open Shrub	Dark Desert	Desert
Bare Soil and Rocks	Barren and Desert	Bright Desert	
Snow and Ice	Snow and Ice	Snow and Ice	Snow and Ice
Water Bodies	Ocean	Ocean	Water

596  
 597  
 598

599

600 Table 3. The various classes for which NTB coefficients are generated.

Parameter	Clear condition	Cloudy condition
Aerosol or cloud type	6 aerosol types (rural, maritime, urban, tropospheric, fog, desert)	3 cloud types (cirrus, stratocumulus, altostratus)
Optical depth (OD)	Typical VIS (km) values for each aerosol types (no OD grid for each aerosol type). Rural: 23, maritime: 23, urban: 5, tropospheric: 50, fog: 0.2, desert: (default VIS for wind speed 10m/s)	Cirrus: [0, 0.8, 1.2, 1.8, 3.2] Stratocumulus: [0, 0.8, 1.2, 1.8, 3.2, 5.8, 8.2, 15.8, 32.2, 51.8, 124.2] Altostratus: [0, 15.0, 30.0, 50.0, 80.0]
Surface type	12 IGBP surface types	4 types (Water, Land, Desert, Snow/Ice)

601

602

603

604

605 Table 4. Angles used in simulations. To be consistent with what is presented in the

606 ABI Shortwave Radiation Budget (SRB) Algorithm Theoretical Basis Documents (ATBD) (Laszlo  
607 et al, 2018) the additional angles used in the simulations are not given in this Table.

Angle Type	Angles
Solar Zenith Angle [°]	0.0, 12.9, 30.8, 41.2, 48.3, 56.5, 63.2, 69.5, 75.5, 81.4, 87.2
Satellite Zenith Angle [°]	0.0, 11.4, 26.1, 40.3, 53.8, 65.9, 76.3
Azimuth Angle [°]	0.0, 1.9, 10.0, 24.2, 44.0, 68.8, 97.6, 129.3, 162.9, 180

608

609

610

611

612

Table 5. MODTRAN simulation speed test (CPU MHz 2099.929).

Algorithm	Stream	Band Resolution (cm <sup>-1</sup> )	Speed (~seconds)
Isaacs	2	1	40
DISORT	2	1, 5, 15	280, 70, 30
	4	1, 5, 15	560, 120, 40
	8	1, 5, 15	930, 300, 110
Scaled	2	1, 5, 15	30, 10, 6.67
Isaac	4	1, 5, 15	30, 10, 6.67
	8	1, 5, 15	30, 10, 6.67

613

614

615

616

617 Table 6. Details on data used as input for calculations.

618

Short Name	Long Name	MODE	ABI-Channel	Scan Sector	Spatial Resolution
RadC	L1b Radiance	M6	C01-C06	CONUS	5000x3000
AODC	L2 Aerosol	M6	--	CONUS	2500x1500
ACMC	L2 Clear Sky Masks	M6	--	CONUS	2500x1500
ACTPC	L2 Cloud Top Phase	M6	--	CONUS	2500x1500
CODC*	L2 Cloud Optical Depth	M6	--	CONUS	2500x1500

619

620 \*The CODC data were not always available from CLASS and had to be obtained from NOAA/STAR  
621 temporary archives. Also, not all the required angular information needed for implementation of the  
622 regressions is available online and had to be re-generated.

623

624

625 Table 7. Statistical summary for all selected cases inter-compared at instantaneous time scale.

Case	CERES	GOES-R	Corr	Bias	Std	RMSE	N
07/31 2019	Terra	G16	0.82	0.81	69.81	69.81	0.22 x10 <sup>6</sup>
		G17	0.87	29.13	90.10	94.70	1.78 x10 <sup>6</sup>
UTC 19	Aqua	G16	0.76	33.87	117.43	122.22	1.58 x10 <sup>6</sup>
		G17	0.78	31.53	129.42	133.21	0.29 x10 <sup>6</sup>
09/13 2019	Terra	G16	0.87	-17.37	81.72	83.54	0.13x10 <sup>6</sup>
		G17	0.71	47.09	108.73	118.48	1.73x10 <sup>6</sup>
UTC 20	Aqua	G16	0.76	18.22	108.50	110.02	1.46x10 <sup>6</sup>
		G17	0.73	25.14	81.95	85.72	0.53x10 <sup>6</sup>
09/21 2019	Terra	G16	0.85	6.78	66.66	67.00	0.35x10 <sup>6</sup>
		G17	0.83	26.41	87.64	91.57	1.75x10 <sup>6</sup>
UTC 19	Aqua	G16	0.82	29.66	105.09	109.20	1.67x10 <sup>6</sup>
		G17	0.76	6.03	94.70	94.89	0.15x10 <sup>6</sup>
09/30 2019	Terra	G16	0.88	4.49	64.79	64.94	0.40x10 <sup>6</sup>
		G17	0.80	19.35	86.41	88.55	1.74x10 <sup>6</sup>
UTC 19	Aqua	G16	0.80	19.87	100.45	102.40	1.69x10 <sup>6</sup>
		G17	0.72	2.71	91.79	91.83	0.12x10 <sup>6</sup>
	Terra	G16	0.86	5.84	51.44	51.77	0.35x10 <sup>6</sup>

10/23		G17	0.87	22.47	70.25	73.76	1.75x10 <sup>6</sup>
2019		G16	0.89	17.10	75.95	77.85	1.67x10 <sup>6</sup>
UTC	Aqua	G17	0.78	8.98	72.52	73.07	0.15x10 <sup>6</sup>
19		G16	0.87	-0.50	43.28	43.28	0.35x10 <sup>6</sup>
11/08	Terra	G17	0.82	17.18	71.27	73.31	1.75x10 <sup>6</sup>
2019		G16	0.90	10.08	71.27	71.98	1.67x10 <sup>6</sup>
UTC	Aqua	G17	0.68	1.53	47.55	47.58	0.15x10 <sup>6</sup>
19		G16	0.79	7.98	49.10	49.75	0.35x10 <sup>6</sup>
11/24	Terra	G17	0.87	14.10	78.35	79.61	1.76x10 <sup>6</sup>
2019		G16	0.82	7.63	58.68	59.17	1.67x10 <sup>6</sup>
UTC	Aqua	G17	0.65	0.19	63.14	63.14	0.15x10 <sup>6</sup>
19		G16	0.88	5.24	53.28	53.54	0.35x10 <sup>6</sup>
12/26	Terra	G17	0.76	11.26	73.95	74.80	1.76x10 <sup>6</sup>
2019		G16	0.83	9.79	58.90	59.56	1.67x10 <sup>6</sup>
UTC 19	Aqua	G17	0.73	0.85	52.53	52.54	0.15x10 <sup>6</sup>

626  
627  
628  
629  
630  
631  
632  
633  
634

635 List of Figures

636 Figure 1. Flowchart of the NTB transformations illustrating the main processing sections.

637 Figure 2. Schematic illustration of the logic employed to synthesize modeled and observed ADMs.

638 Figure 3. The location of the 100 selected clear sky profiles from SeeBor used in the simulations.

639 Figure 4. Profile statistics of: (a) temperature; (b) water vapor; (c) ozone for the entire available sample  
640 and for the reduced sample used in this study. Error bar is 1 standard deviation.

641 Figure 5. Re-mapped IGBP surface classifications over the CONUS at 2-km ABI grid.

642 Figure 6. Simulated Radiances from DISORT 8-stream (with 1, 5, and 15  $\text{cm}^{-1}$  resolution band model  
643 for spectral range of 0.4 – 0.5  $\mu\text{m}$  (left) and 1.5 – 2.0  $\mu\text{m}$  (right).

644 Figure 7. Radiance differences between various multi-scattering algorithms and DISORT-8 stream.

645 *Upper*: the whole simulated spectrum of 0.2-4  $\mu\text{m}$ ; *Lower*: zoom on 0.3-0.35  $\mu\text{m}$  (Relative  
646 Azimuthal Angle=1.9°, View Angle=76.3°, Solar Zenith Angle=87.2°).

647 Figure 8. Locations of the six ABI channel SRFs. X-axis is wavenumber. Y-axis is solar irradiance.

648 Figure 9. Comparison of TOA flux from ABI and CERES FLASHFlux for 2017/11/25, 17:57Z. (a)  
649 CERES Terra product; (b): results with “separate-channel” coefficients. (c): difference (ABI-  
650 CERES); (d): histogram of ABI-CERES differences (this is the only case illustrated in this paper  
651 with data from FLASHFlux)

652 Figure 10. Statistics for relative Bias and RMSE. The y-axis is percentage. The x-axis is the case used in  
653 the inter-comparison. Blue - cloudy orange - clear sky and t gray - all sky.

654 Figure 11. (a) All sky TOA SW from CERES\_SSF/Aqua, (b) CERES\_SSF/Terra, (c) re-gridded  
655 CERES\_SSF/Aqua, (d) re-gridded CERES\_SSF/Terra, (e) GOES-16 and (f) GOES-17 on  
656 12/26/2019 at UTC 19:36.

657 Figure 12. (a) Frequency distribution of all-sky TOA SW differences between ABI on GOES-16 and  
658 CERES, (b) ABI on GOES-17 and CERES\_SSF using Aqua (Upper) and Terra (Lower). All  
659 observations were used (clear and cloudy) on 12/26/2019 at UTC 19:36.

660 Figure 13. Same as Figure 11 but for clear TOA SW differences.



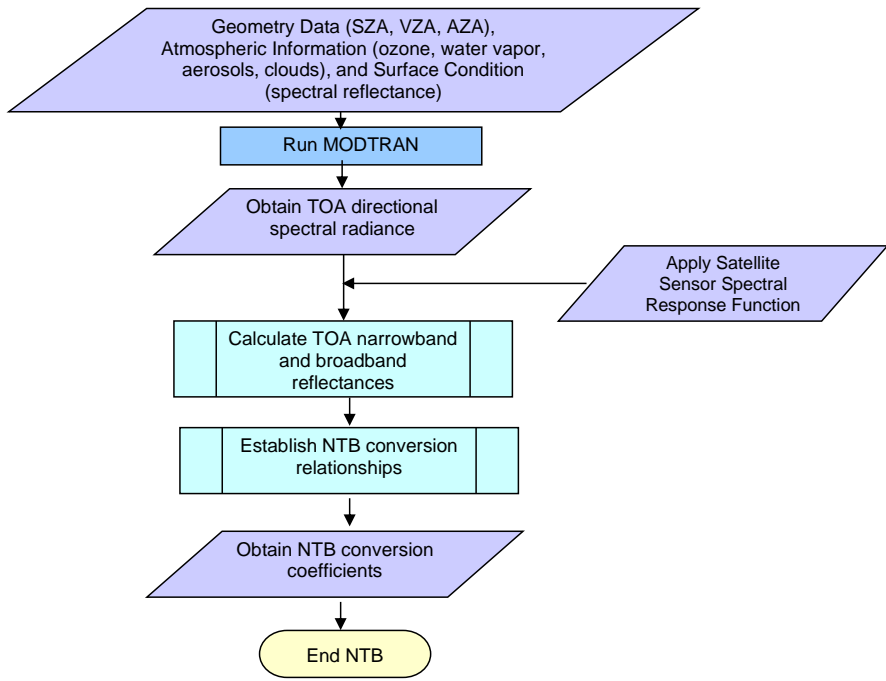
661 Figure 14. Same as Figure 11 but for cloudy TOA SW differences.

662 Figure 15. *Left:* Sensor response function for ABI channel 6; *Right:* Spectral albedo for desert and open  
663 shrubs. Desert albedo value is much higher than open shrubs at 2.2  $\mu\text{m}$ .

664  
665  
666  
667  
668  
669  
670  
671  
672  
673  
674  
675  
676  
677  
678  
679  
680  
681  
682  
683  
684  
685  
686  
687  
688  
689  
690  
691  
692  
693  
694  
695  
696  
697

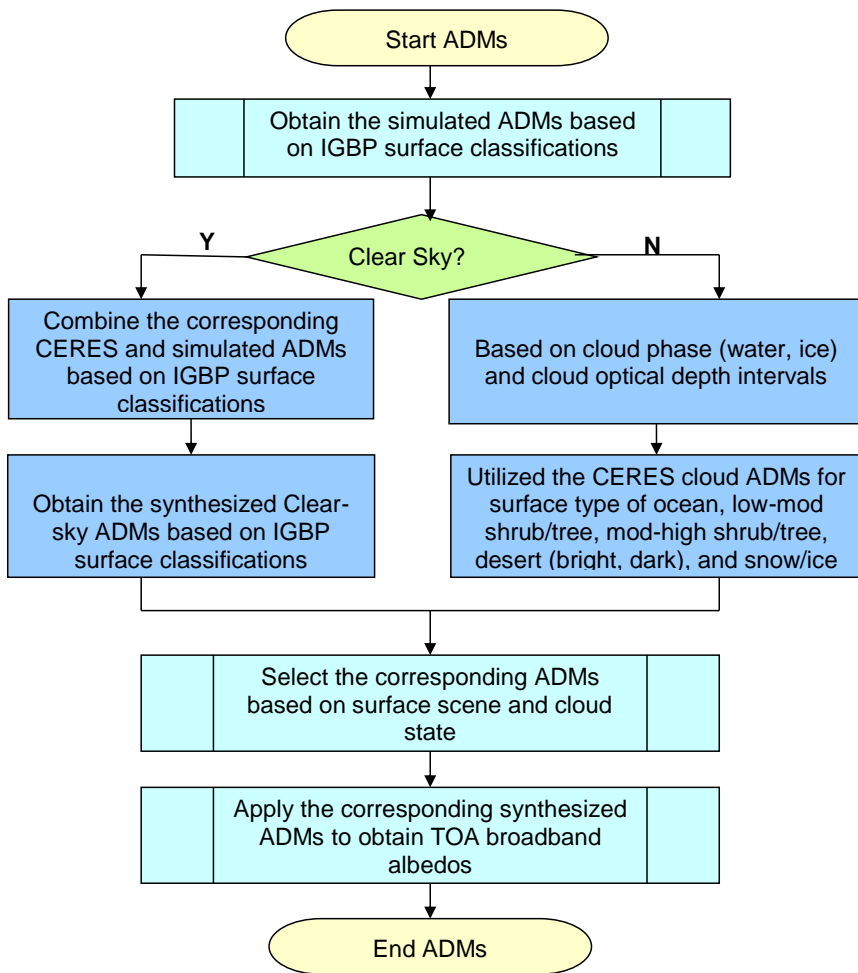
698 **Figures**

699  
700



701  
702 Figure 1. Flowchart of the NTB transformations illustrating the main processing sections.

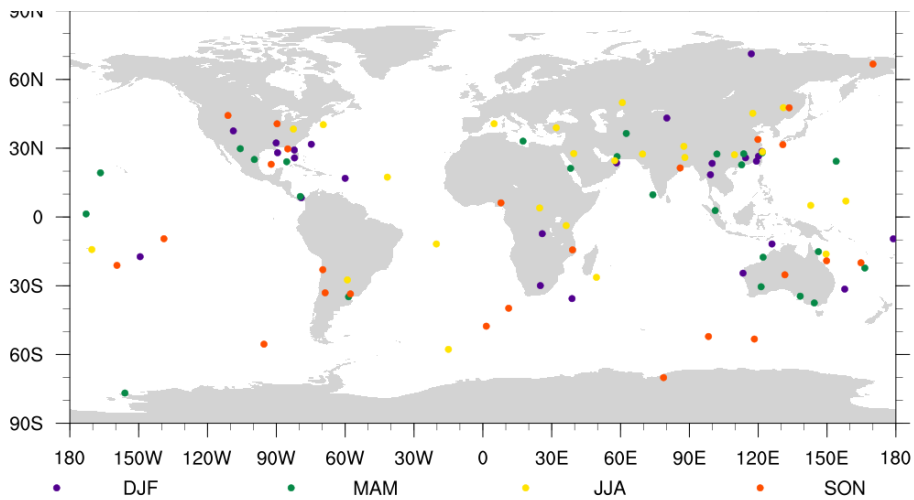
703  
704  
705



706

707 Figure 2. Schematic illustration of the logic employed to synthesize modeled and observed ADMs.

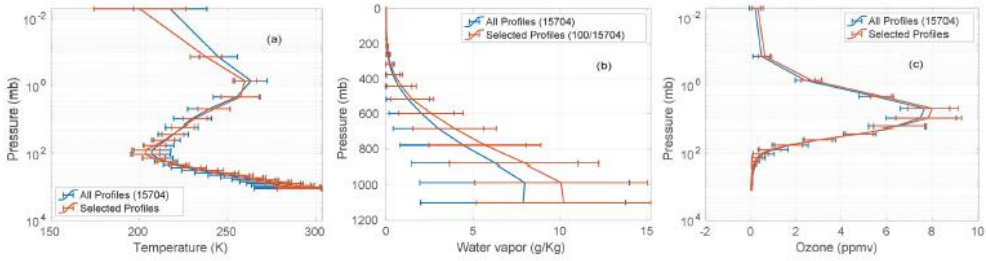
708  
709  
710  
711



712  
713  
714

Figure 3. The location of the 100 selected clear sky profiles from SeeBor used in the simulations.

715



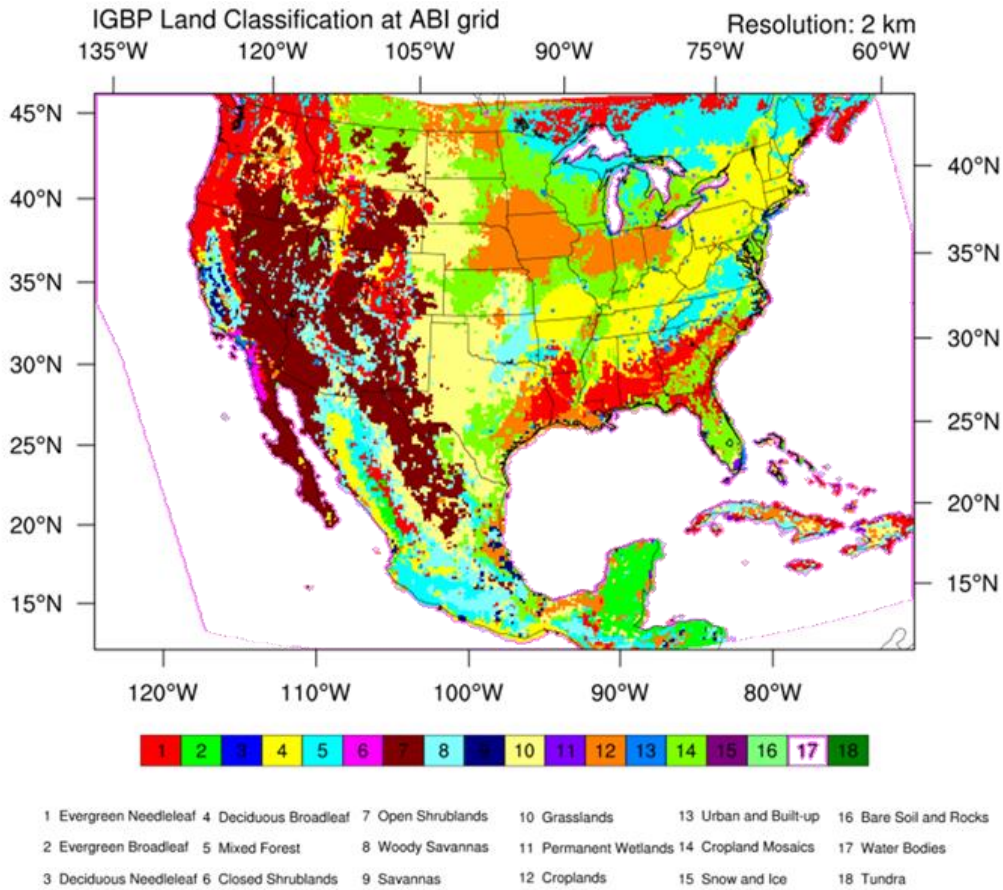
716

717 Figure 4. Profile statistics of: (a) temperature; (b): water vapor; (c) ozone for the entire available sample  
718 and for the reduced sample used in this study. Error bar is 1 standard deviation.

719

720

721



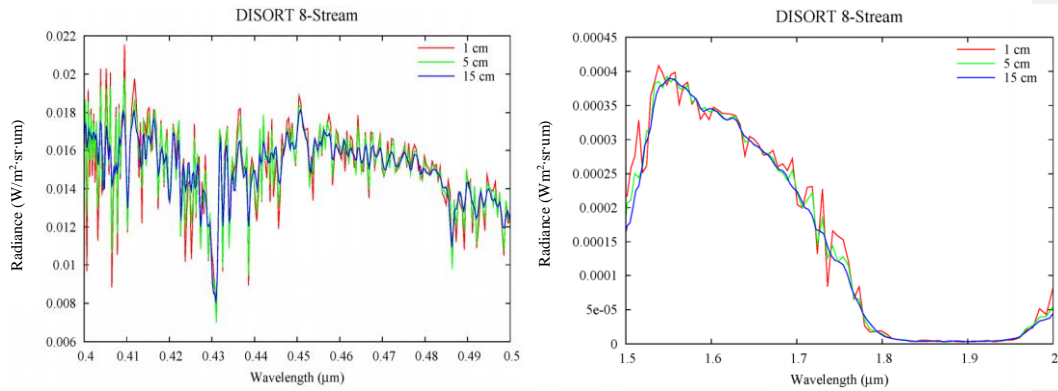
722

723 Figure 5. Re-mapped IGBP surface classifications over the CONUS at 2-km ABI grid.

724

725

726



727

728

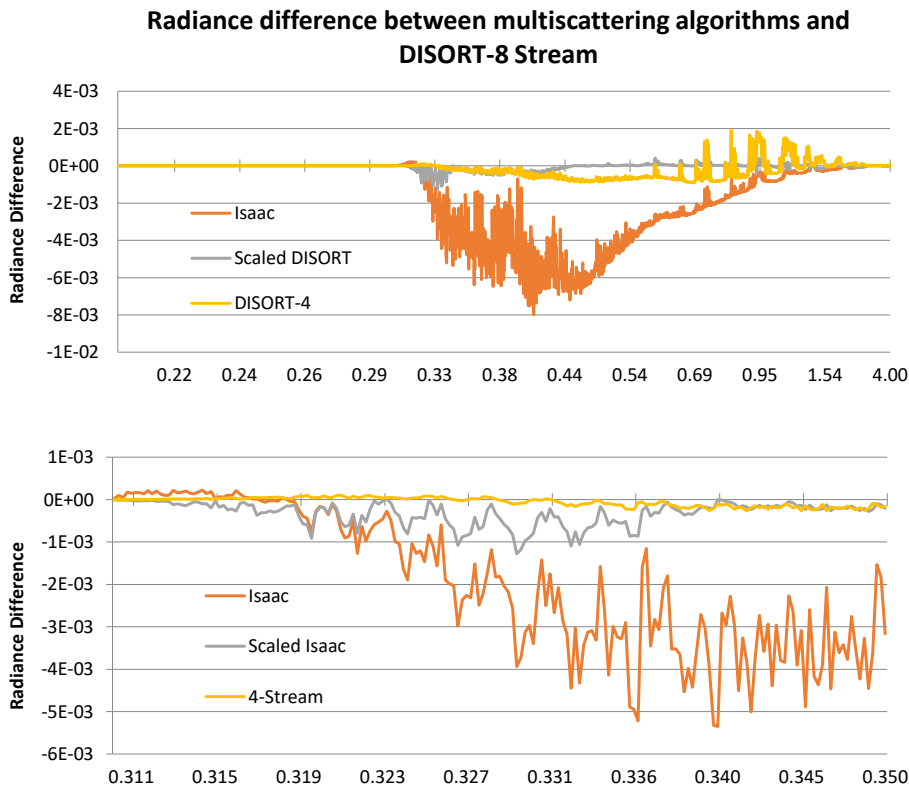
729

730

731

Figure 6. Simulated Radiances from DISORT 8-stream (with 1, 5, and 15 cm<sup>-1</sup> resolution band model for spectral range of 0.4 – 0.5 μm (left) and 1.5 – 2.0 μm (right).

732  
733

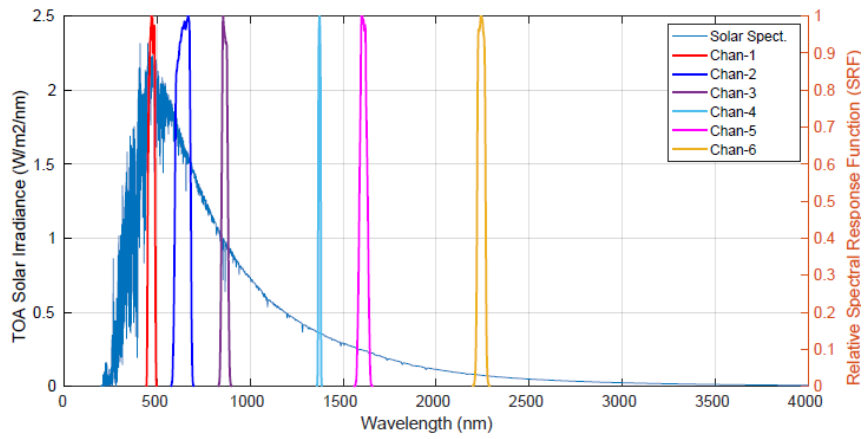


734

735  
736  
737  
738  
739

Figure 7. Radiance differences between various multi-scattering algorithms and DISORT-8 stream.  
*Upper:* the whole simulated spectrum of 0.2-4  $\mu\text{m}$ ; *Lower:* zoom on 0.3-0.35  $\mu\text{m}$  (Relative Azimuthal Angle=1.9°, View Angle=76.3°, Solar Zenith Angle=87.2°).





740

741

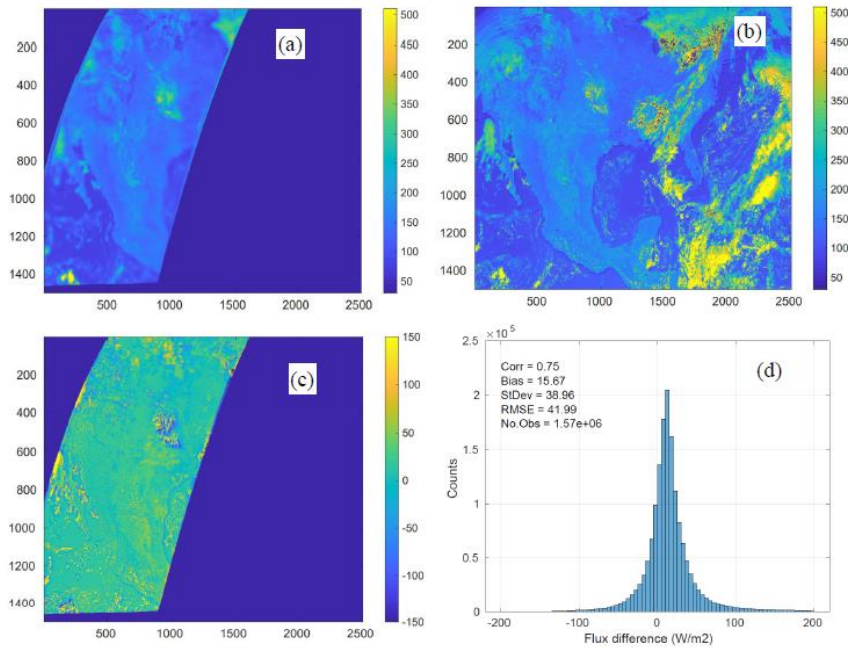
742 Figure 8. Locations of the six ABI channel SRFs. X-axis is wavenumber. Y-axis is solar irradiance.

743

744

745

746



747

748 Figure 9. Comparison of TOA flux from ABI and CERES FLASHFlux for 2017/11/25, 17:57Z. (a)

749 CERES Terra product; (b): results with “separate-channel” coefficients. (c): difference (ABI-

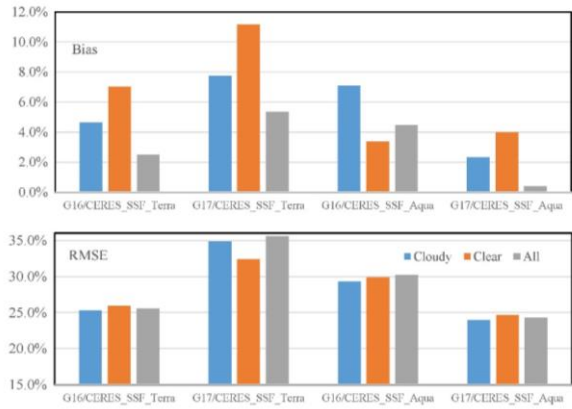
750 CERES); (d): histogram of ABI-CERES differences (this is the only case illustrated in this paper

751 with data from FLASHFlux).

752

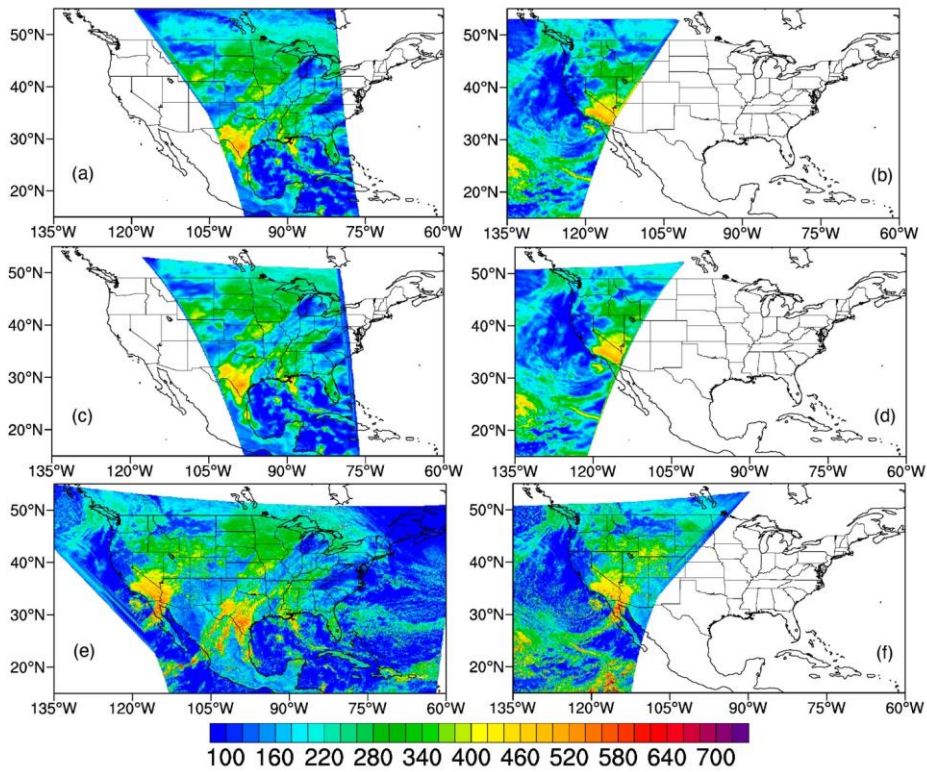
753

754

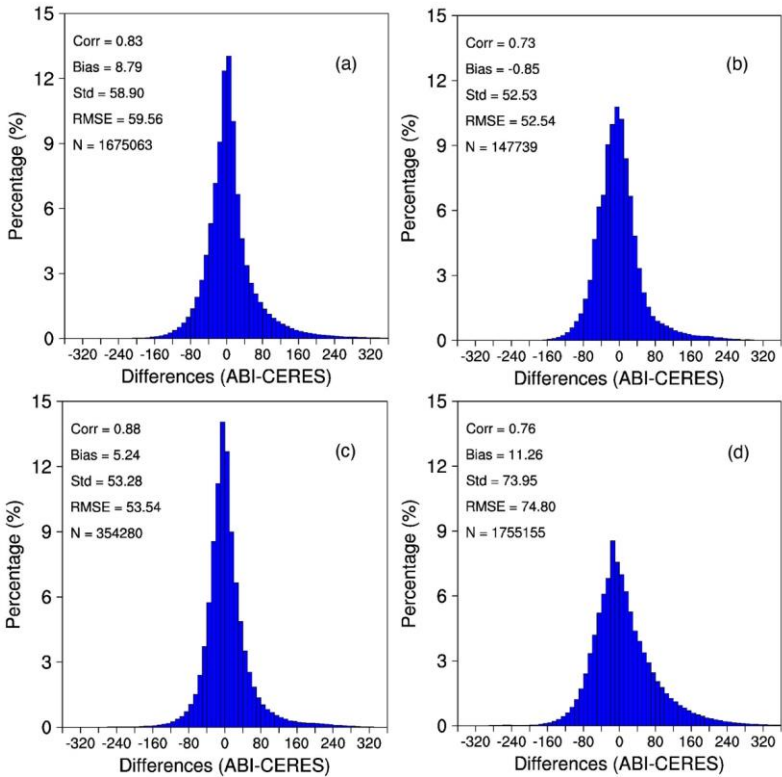


755  
756  
757  
758  
759  
760  
761  
762  
763  
764  
765  
766  
767

Figure 10. Statistics for relative Bias and RMSE. The y-axis is percentage. The x-axis is the case used in the inter-comparison. Blue - cloudy orange - clear sky and t gray - all sky.



768  
 769  
 770 Figure 11. (a) All sky TOA SW from CERES\_SSF/Aqua, (b) CERES\_SSF/Terra, (c) re-gridded  
 771 CERES\_SSF/Aqua, (d) re-gridded CERES\_SSF/Terra, (e) GOES-16 and (f) GOES-17  
 772 on 12/26/2019 at UTC 19:36.



777

778

779

780

781

Figure 12. (a) Frequency distribution of all-sky TOA SW differences between ABI on GOES-16 and CERES, (b) ABI on GOES-17 and CERES\_SSF using Aqua (Upper) and Terra (Lower). All observations were used (clear and cloudy) on 12/26/2019 at UTC 19:36.

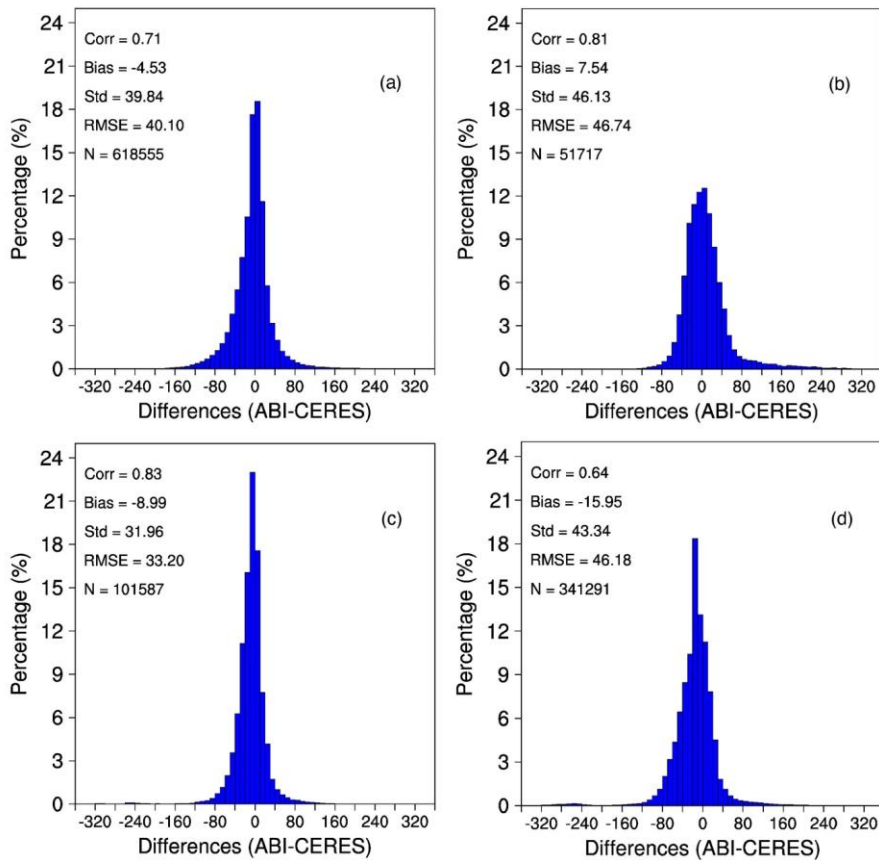


Figure 13. Same as Figure 11 but for clear TOA SW differences.

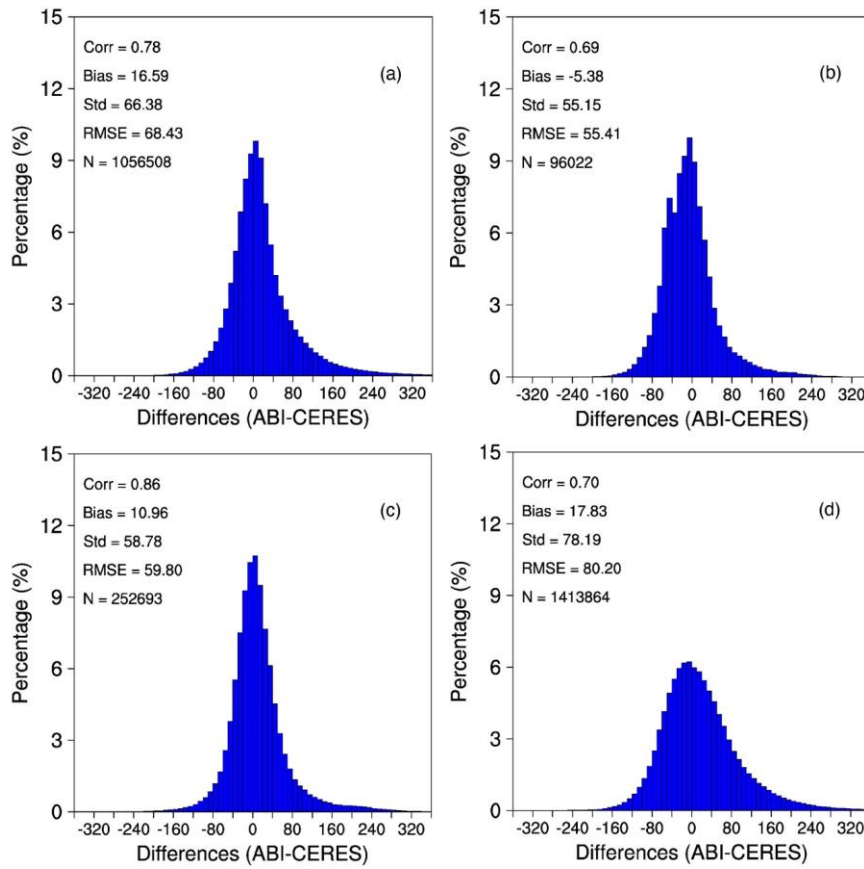
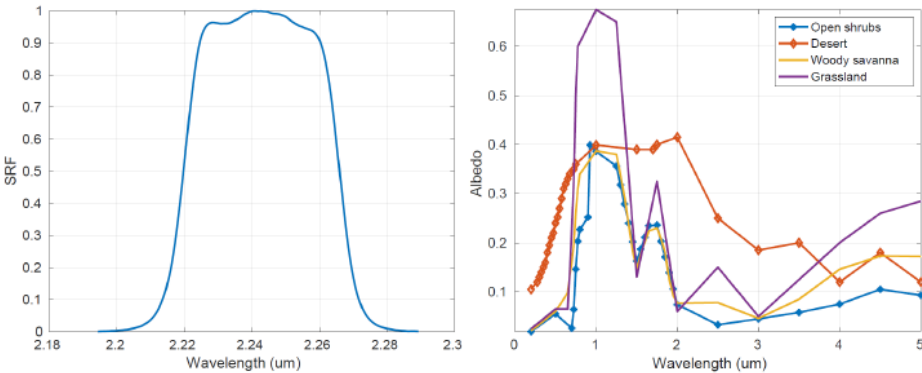


Figure 14. Same as Figure 11 but for cloudy TOA SW differences.

785  
786  
787  
788

789



790

791 Figure 15. *Left:* Sensor response function for ABI channel 6; *Right:* Spectral albedo for desert and open  
792 shrubs. Desert albedo value is much higher than open shrubs at 2.2 μm.

793

794